Time–frequency control of ultrafast plasma generation in dielectrics

Jiexi Liao and Jeremy R. Gulley*

Department of Biology and Physics, Kennesaw State University, Kennesaw, Georgia 30144, USA
**Corresponding author: jgulley@kennesaw.edu*

Received August 19, 2014; revised October 5, 2014; accepted October 8, 2014;
posted October 14, 2014 (Doc. ID 221200); published November 7, 2014

This paper examines ultrafast laser-induced plasma generation in dielectrics by modeling ionization and pulse propagation in glass. Photoionization models for solids predict that the multi-photon ionization rate should increase for near-UV frequencies when compared to those in the visible or near-IR. Conversely, the frequency dependence of a Drude-type absorption by free electrons can produce an increased ionization yield through avalanching for frequencies in the IR. The simulations presented in this paper reveal how such frequency-dependent models influence the plasma formation during nonlinear pulse propagation in fused silica. It is further shown by a multi-rate equation model that the contribution from avalanching, when properly delayed, is reduced by an order of magnitude at near-IR frequencies throughout the propagation. A modified multi-rate equation is then introduced to model combinations of ultrashort high-frequency and low-frequency pulses that can maximize plasma generation while operating at the lowest possible fluences. © 2014 Optical Society of America

OCIS codes: (190.5530) Pulse propagation and temporal solitons; (190.7110) Ultrafast nonlinear optics; (260.3230) Ionization; (320.7130) Ultrafast processes in condensed matter, including semiconductors.
http://dx.doi.org/10.1364/JOSAB.31.002973

1. INTRODUCTION

Femtosecond laser pulses can affect material modifications on the submicrometer scale and with greater precision than longer pulses [1,2]. This is partially due to the fact that ultrashort pulses provide high intensities sufficient for optical breakdown with minimal fluence. It is also due to the sample's exposure time being shorter than that required for most thermal effects [3]. Ultrashort laser pulses and their interaction with materials have been studied extensively [4], and yet a practical ionization model to account for the multi-frequency nature of ultrashort pulses remains elusive [5]. Ultrafast plasma generation typically begins with photoionization (PI) and progresses to free-carrier absorption, leading to impact ionization and avalanching [6]. Understanding how this process depends simultaneously on the time and frequency arrangement of the pulse may enable one to customize laser fields to control laser-induced ionization [7–9] in applications, such as micromachining [10–14], nanometer scale medical procedures [15], and directed energy [16].

When coupled with pulse propagation simulations, plasma formation may be modeled by a single rate equation (SRE) [17] that describes the time evolution of the plasma density ρ and is given by

$$\frac{d\rho}{dt} = W_{\mathrm{PI}}(I,\omega) + \frac{\sigma I}{\epsilon_{\mathrm{crit}}}\rho - \frac{\rho}{\tau_{\mathrm{r}}}. \tag{1}$$

Here, the photoionization term W_{PI} is calculated using the complete Keldysh model [18], which combines the multi-photon and tunneling ionization mechanisms to calculate the PI rate. The variables I and ω are the optical intensity and frequency, respectively. The second term accounts for electron avalanching, where

$$\sigma = \frac{1}{n_0 c\epsilon_0}\frac{e^2\tau_{\mathrm{c}}}{m(1+\omega^2\tau_{\mathrm{c}}^2)} \tag{2}$$

is the cross section of inverse bremsstrahlung absorption as calculated by the Drude model [19,20] and n_0 is the linear index of refraction. In Eq. (1), the energy $\epsilon_{\mathrm{crit}} = U_{\mathrm{eff}}(1 + m/m_{\mathrm{e}})$ is the critical energy for impact ionization [21], m_{e} is the free electron mass, $U_{\mathrm{eff}} = U + e^2|A|^2/(4m\omega^2)$ is the effective bandgap including the ordinary material bandgap U and the ponderomotive energy of the free-carrier, and $|A|$ is the laser field amplitude. The final term in Eq. (1) corresponds to decay resulting from recombination events [22].

Equation (1) couples to the optical field only in the first two terms on the right-hand side. The photoionization term is intrinsically nonlinear in the intensity for dielectrics, i.e., assuming that $U > \hbar\omega$. The avalanching term appears linear in the intensity but is indirectly nonlinear in that the time evolution of ρ also depends on the optical intensity. The efficiency of the avalanching term is largely determined by the cross section σ, which in turn depends on the relation between the optical frequency and the chosen collision time τ_{c}. This is demonstrated graphically in Fig. 1(a) which plots σ as a function of the collision time and laser wavelength. Figure 1(a) indicates that, for the range of collision times typically used (0.2–20 fs [20]), higher wavelength fields can drive the avalanching process more efficiently once seed electrons are provided. However, it should also be noted that as the wavelength increases, so does the effective bandgap and the critical energy for avalanching ϵ_{crit} in Eq. (1). This effect can conversely reduce the influence of avalanching at higher wavelengths and intensities.

Seed electrons are provided by the photoionization term in Eq. (1), which is plotted in Fig. 1(b) as a function of laser intensity and wavelength. From Fig. 1(b) one can clearly

 © 2014 Optical Society of America

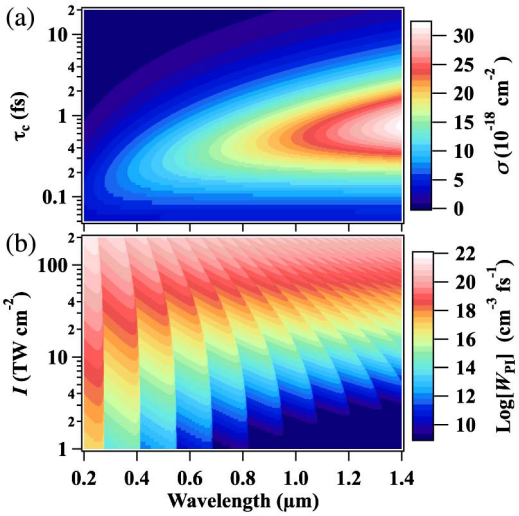

Fig. 1. (a) Drude absorption cross section as a function of collision time and wavelength. (b) Keldysh photoionization rate as a function of intensity and wavelength for a 9 eV bandgap material.

distinguish separate multi-photon ionization (MPI) domains bounded where the number of photons required for an MPI event increases or decreases by one integer value. Crossing one of these MPI boundaries on the plot (which vary as functions of intensity and frequency) often changes the resultant rate by an order of magnitude or more compared to the rate at the same intensity but slightly different wavelength on the other side of the border, or vice versa. For the wavelengths shown in Fig. 1(b), the various MPI domains at shorter wavelengths have higher PI rates since they require fewer photons per absorption event.

Therefore, the respective plasma generation processes of PI and avalanching tend to be more efficient at opposite ends of the visible spectrum. This paper addresses the consequences of this frequency dependence for pulses of various time durations using Eq. (1) combined with standard pulse propagation simulations. It also addresses how these effects depend on the pulse width and wavelength arrangement of the laser fields, and reveals plasma dynamics that require an improvement to Eq. (1) via a multi-rate equation approach. For the case of NIR pulses, the multi-rate equation model shows that the avalanche effect, when properly delayed, results in an ionization yield differing by about an order of magnitude when compared to the yield predicted by Eq. (1). Optimal wavelength and pulse width conditions for plasma generation are determined for single-pulse fields of high and low fluence. The paper concludes by introducing a modified multi-rate equation to model double-pulse trains containing two different frequencies. This model shows how multi-chromatic double-pulse trains can control plasma generation on ultrashort time scales by increasing the ionization yield with a reduced fluence.

2. FREQUENCY DEPENDENCE OF PLASMA GENERATION

This section examines the time–frequency dependence of ultrafast plasma generation using simulations of pulse propagation through a 10 μm penetration depth of fused silica. There are several advantages of using multidimensional propagation simulations for this purpose. First, one can observe plasma generation not only at the beam peak on-axis, but also everywhere along the beam structure where the pulse has lower intensities. Therefore, if the changing beam intensity crosses the boundary of an MPI domain [see Fig. 1(b)] then this will be represented in the ionization yield throughout the beam. Second, one can see how quickly the linear optics (dispersion and diffraction) and nonlinear optics (the Kerr effect and plasma effects) affect plasma formation in the sample [23,24]. Third, one directly observes how well the plasma formation is localized in 3D space [25], which is important in the context of laser-machining applications.

Table 1. Pulse Parameters for Propagation Simulations

	Energy (μJ)	Pulse Width (fs)	Beam Width (μm)	Peak Intensity (TW/cm^2)
Case 1	2	100	10	12
Case 2	1	50	10	12

The propagation simulations are performed for the common laser wavelengths of 400, 532, 800, and 1064 nm. For each wavelength two simulations are performed: one for a pulse of 2 μJ energy and 100 fs FWHM pulse width, referred to as case 1, and the other for a pulse of 1 μJ energy and 50 fs FWHM pulse width, referred to as case 2. Each pulse starts with a $1/e^2$ spot size of 10 μm on the sample surface. These cases are summarized in Table 1 for later reference. The pulses are assumed to have transform-limited Gaussian beam and pulse shapes at the surface.

The propagation simulations solve a modified nonlinear Schrödinger equation for the electric field envelope $A(x, y, z, \tau)$ traveling in the frame of the laser pulse moving at the group velocity [20]

$$\frac{\partial A}{\partial z} = \frac{i}{2k_0}\hat{T}^{-1}\nabla_\perp^2 A + i\hat{D}_b A + i\frac{k_0 n_2}{n_0}(1-f_r)\hat{T}[IA] + i\frac{k_0 n_2}{n_0}f_r\hat{T}\left[\int_{-\infty}^{\tau} d\tau' R(\tau-\tau')I(\tau')\right]A - \frac{W_{PI}U}{2I}A - \frac{\sigma}{2}(1+i\omega_0\tau_c)\hat{G}^{-1}[\rho A]. \quad (3)$$

This equation is solved using a split-step method with a fast Fourier transform to evaluate all spatial and time derivatives. All constants for the material are taken from Ref. [22], and the linear refractive index is calculated by a Sellmeier equation. The formulas, operators, and values used in Eq. (3) are defined and summarized in Table 2. Equation (3) is solved simultaneously with Eq. (1) for the plasma density.

After simulated propagation through the medium, the maximum plasma produced by ionization at each position in the material for cases 1 and 2 are shown in Figs. 2 and 3 as a function of beam position and propagation distance. Since PI rates tend to be higher for higher frequencies, it is commonly assumed that resulting ionization yields should also be greater for higher frequencies. However, the maximum ionization yield in Fig. 2 occurs not for the 400 nm pulse, but for the 1064 nm pulse. For the intermediate wavelengths 532 and 800 nm the yields are comparatively lower.

It is notable that the 1064 nm pulse has the lowest PI rate out of the four wavelengths, while the Drude absorption cross section $\sigma(\omega)$ is largest in this wavelength range (see Fig. 1).

Table 2. Formulas and Values Used in Eq. (3) [20]

	Description	Definition or Value
λ	Peak laser wavelengths	400, 532, 800, and 1064 nm
ω_0	Carrier frequency	$2\pi/\lambda$
I	Intensity	$I = (1/2)n_0 c\epsilon_0 \lvert A\rvert^2$
z	Propagation axis	
τ	Retarded time	$\tau = t - zk_1$
k	Wave vector	$k(\omega) = n(\omega)\omega/c$
k_m	Dispersion coefficients	$k_m = \frac{\partial^m k(\omega)}{\partial \omega^m}\lvert_{\omega_0}$
$\hat{D}_b$	Bound charge linear dispersion operator	$\hat{D}_b = \sum_{m=2}^{\infty} \frac{k_m}{m!}(i\partial_\tau)^m$
$\hat{T}$	Steepening operator	$\hat{T} = 1 + i\frac{1}{\omega_0}\partial_\tau$
$\hat{G}$	Drude dispersion operator	$\hat{G} = 1 + \frac{i}{\omega_0} g\partial_\tau$
g	Drude dispersion coefficient	$g = (-i\omega_0\tau_c)/(1 - i\omega_0\tau_c)$
$R(\tau)$	Raman response function	$R(\tau) = \frac{\tau_1^2+\tau_2^2}{\tau_1\tau_2^2} e^{-\tau/\tau_2} \sin \tau/\tau_1$
τ_1	Raman response time	32 fs
τ_2	Raman response time	12.2 fs
f_r	Raman fraction of the nonlinear polarization	0.18
n_2	Nonlinear refractive index	2.48×10^{-16} cm^2 W^{-1}
U	Bandgap energy	9 eV
m_e	Electron mass	9.1×10^{-31} kg
m	Reduced electron-hole mass	$0.5m_e$
τ_c	Electron collision time	1.2 fs

According to Fig. 2, the 1064 nm pulse generates an ionization yield an order of magnitude higher than that of the 400 nm pulse, but that yield quickly declines after 1 μm of propagation. The high yield for the 1064 nm pulse occurs primarily due to the influence of avalanching. However, its strong localization along the propagation axis to about 1 μm is due to photoionization being more strongly nonlinear for the NIR pulse than any of the others. The plasma generated by the 400 nm pulse, by contrast, remains quite consistent throughout the 10 μm of propagation. The intermediate wavelength cases show lower yields, but the 800 nm case is the more effectively localized along the beam dimensions.

The influence of the avalanche process is also sensitive to the pulse's time duration. The shorter 50 fs laser pulse from

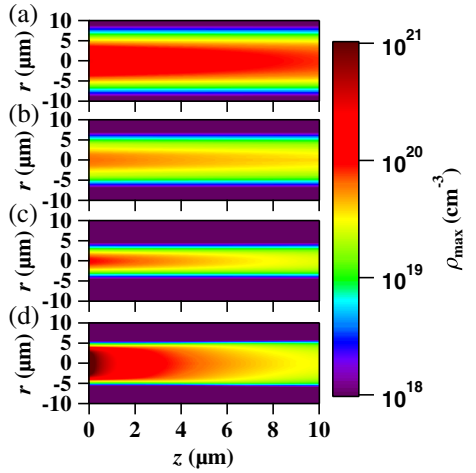

Fig. 2. Maximum plasma density as a function of beam position r and propagation distance z for a 2 μJ pulse of wavelength (a) 400, (b) 532, (c) 800, and (d) 1064 nm. Equation (1) was used to calculate the plasma evolution.

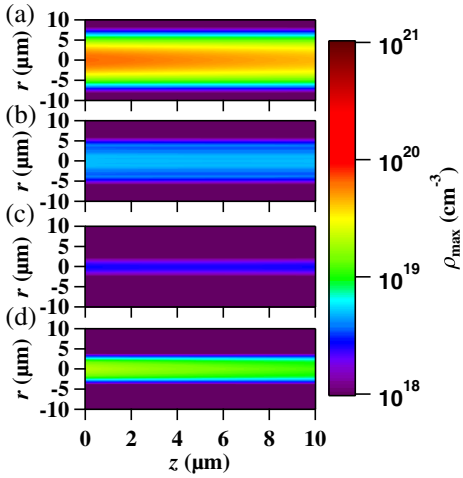

Fig. 3. Maximum plasma density as a function of beam position r and propagation distance z for a 1 μJ pulse of wavelength (a) 400, (b) 532, (c) 800, and (d) 1064 nm. Equation (1) was used to calculate the plasma evolution.

case 2 will not have as much time or energy to exponentially increase the ionization yield by avalanching. Figure 3 shows the maximum plasma densities generated by the case 2, 1 μJ pulses. While the 800 and 532 nm wavelength plasma densities are again lower than those of the 1064 and 400 nm data, the maximum ionization yield occurs for 400 nm instead of 1064 nm due to the reduction in the free-carrier absorption rate. This fact makes the accurate calculation of avalanching for NIR fields extremely important. Equation (1) is the most common model of plasma generation coupled with pulse propagation [26]. It is a highly advantageous model because it is simple, easily interpretable, and imposes a minimal computational burden. However, more recently proposed models [27,28] show that ultrafast avalanching is not only reduced by the reduction of pulse width, but also delayed from the onset of photoionization since electrons take a finite time to absorb the critical energy before impact ionization occurs [6]. The influence of this delay in the final ionization yield and its dependence on pulse frequency is explored in the next section.

3. TIME DEPENDENCE OF PLASMA GENERATION

A. Delayed Effect of Avalanching

Simple descriptions of impact ionization on the femtosecond scale often use one of two models: an SRE [see Eq. (1)] [17,29] or a multi-rate equation (MRE) [28] for electrons in the conduction band. The MRE differs from the SRE by modeling the transient electron energy distribution and captures the delay of the electron avalanche effect [28]. The MRE discretizes the conduction band into energy bins ϵ_n of width $\Delta\epsilon = \hbar\omega$, where ω is the pulse frequency. The density of electrons in each bin ρ_n is evolved by its own rate equation coupled to those of the other bins. Photoionization places electrons in the lowest energy bin initially. The carriers then experience one-photon absorption events, each time advancing one bin further up in energy. This continues until the electrons reach the critical energy required for impact ionization, at which point this work assumes an immediate impact ionization event will occur [27]. This results in a delay of the avalanche effect, since

only electrons that have absorbed the critical energy can cause impact ionization. The SRE, by contrast, allows all electrons to immediately participate in impact ionization regardless of their energy.

Defining ρ_n as the density of electrons in the energy range $\epsilon_n = n\hbar\omega + \Delta\epsilon$, the plasma is evolved according to the following MRE:

$$\frac{d\rho_n}{dt} = W_{\mathrm{PI}}(I,\omega)\delta_{n0} - \frac{\rho_n}{\tau_r} + \frac{\sigma(\omega)I}{\hbar\omega}[\rho_{n-1} - \rho_n + D_{nk}\rho_{k-1}], \quad (4)$$

where $k = \langle \epsilon_{\mathrm{crit}}/\hbar\omega + 1\rangle$ is the number of single-photon absorption events required for impact ionization, $\langle\cdot\rangle$ again denotes the integer part, δ_{nm} is the Kronecker delta, and θ_{nm} is the step function defined as $\theta_{nm} = \{1 \text{ for } n \geq m,\ 0 \text{ otherwise}\}$. For notational simplicity, ρ_n and its time rate of change are defined to be zero for all $n < 0$.

All electrons being transferred into energy bins at level ϵ_k or above are assumed to immediately result in impact ionization. To conserve energy and momentum during the impact ionization process we use the approach given in [30]. Here the energy-dependent distributing function for impact ionization contributions to the MRE is defined as

$$D_{nl} = \Upsilon\left(\frac{\epsilon_l^{\mathrm{imp}} - \epsilon_n}{\Delta\epsilon}\right)\theta_{lk}, \quad (5)$$

where $\epsilon_l^{\mathrm{imp}} = (\epsilon_l - U_{\mathrm{eff}})/3$ is the resultant energy of both electrons after impact ionization involving an electron from energy bin ϵ_l and a valance electron. Since $\epsilon_l^{\mathrm{imp}}$ takes on continuous values, the resultant contributions are distributed among the energy bins according to the function [24]

$$\Upsilon(x) = \begin{cases} 2 & \text{for } 0 \leq |x| \leq 0.25, \\ 1 & \text{for } 0.25 < |x| < 0.75, \\ 0 & \text{else.} \end{cases}$$

During the plasma evolution as modeled by Eq. (4), some electrons at energies greater than ϵ_k may be exist from an earlier time when ϵ_{crit} was higher. When such cases occur this work assumes that the electrons in these levels immediately impact ionize and are redistributed, along with former valance electrons, according to Eq. (5).

To examine the effect of avalanche delay for different frequencies this section models plasma generation with the SRE and MRE and compares the results. These calculations use the on-axis fields for cases 1 and 2 as described in Section 2, Table 1, and use the same laser wavelengths of 400, 532, 800, and 1064 nm. Results for the case 1 pulses are shown in the top row of Fig. 4 and the case 2 pulses are shown in the bottom row. The SRE calculations are in the left column of Fig. 4 and the MRE calculations are in the right column. The plasma densities calculated using a MRE are less than those calculated using a SRE by a factor of 2–10, with cases of higher energy and longer wavelength showing greater difference between the two methods as demonstrated in earlier works [28]. In particular, the NIR fields show nearly an order of magnitude difference, or more, for each case. The results confirm that the SRE method overestimates the ultrafast plasma generation for the cases under study, especially for lower frequency fields.

Also examined is the use of the MRE in place of the SRE in the propagation simulations of Section 2. The maximum plasma densities during the propagation are plotted in Figs. 5 and 6. Note that the total ionization yield is reduced in all cases by assuming the MRE model. In particular, the ionization yields of the near-IR pulses are reduced by approximately an order of magnitude throughout the propagation by switching from the SRE to the MRE. Nevertheless, the general trends demonstrated by the SRE model remain. For the high-energy pulses, the 1064 nm pulse generates the highest yields, followed by that of the 400 nm pulse. Again, the 1064 and 800 nm pulse ionization yields are the most effectively localized along the propagation axis and beam axis, respectively.

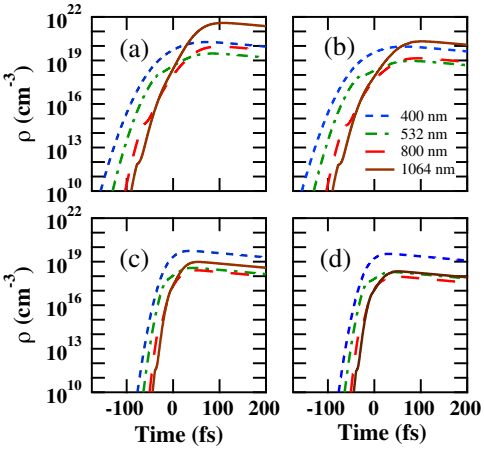

Fig. 4. Plasma density as a function of time for 400, 532, 800, and 1064 nm pulses of 100 fs, 2 μJ using the (a) SRE method and (b) MRE method and pulses of 50 fs, 1 μJ using the (c) SRE method and (d) MRE method.

B. Optimal Pulse Width and Frequency Combinations for Single-Pulse Ionization with a Fixed Fluence

Single-shot damage thresholds are often given in terms of the incident laser energy per area, or fluence. As has been previously shown [31], this is not an ideal description for ultrafast laser-induced damage. The problem can be theoretically examined by calculating the maximum ionization yields generated on the dielectric surface as a continuous function of both wavelength and pulse width (see Fig. 7). These calculations model plasma generation using the MRE and the

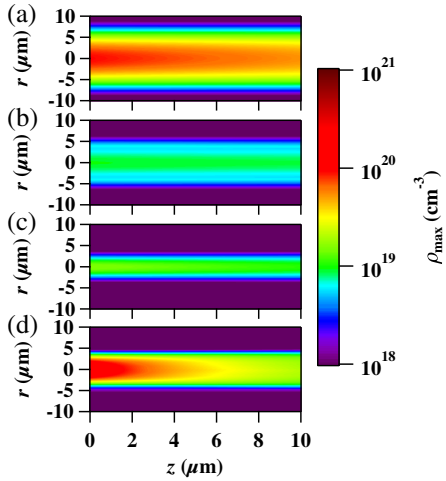

Fig. 5. Maximum plasma density as a function of beam position r and propagation distance z for a 2 μJ pulse of wavelength (a) 400, (b) 532, (c) 800, and (d) 1064 nm. Equation (4) was used to calculate the plasma evolution.

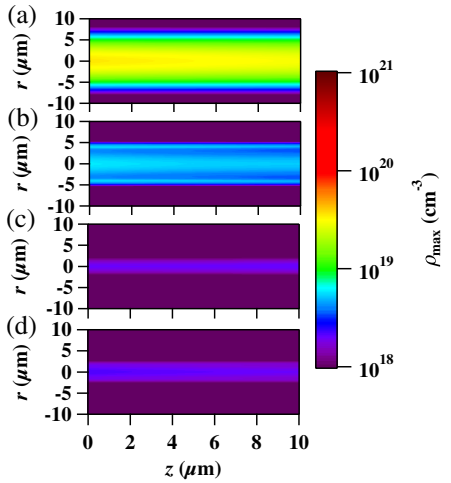

Fig. 6. Maximum plasma density as a function of beam position r and propagation distance z for a 1 μJ pulse of wavelength (a) 400, (b) 532, (c) 800, and (d) 1064 nm. Equation (4) was used to calculate the plasma evolution.

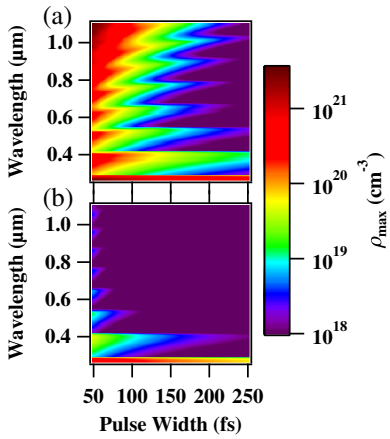

Fig. 7. Maximum plasma density generated in fused silica as a function of wavelength and pulse width for a pulse with energy (fluence) of (a) 2 μJ (2 J/cm^2) and (b) 1 μJ (1 J/cm^2).

energies and beam width used formerly in case 1 [Fig. 7(a)] and case 2 [Fig. 7(b)] as summarized in Table 1. Therefore, all data points on either plot were calculated using the same fluence. However, note that since the pulse width is allowed to vary, the peak intensity of the pulse varies accordingly. It is this coupled variation in pulse width and intensity that changes the ionization yield by orders of magnitude. Since all the points in each plot have the same fluence, these results support the general agreement that thresholds for ultrafast ionization, and any resulting damage, must be specified with a combined fluence and temporal width; or alternatively pulse width and peak intensity.

The step-like shapes seen in Fig. 7 result from the intensity and frequency dependence of photoionization [see Fig. 1(a)]. For the higher fluence case, Fig. 7(a), it is notable that in the 150–250 fs pulse width range at higher wavelengths the step-like shape becomes less definite, indicating that impact ionization dominates both the quantitative value and qualitative behavior of plasma generation in this range of parameters. These results also compare well with experiment, which shows damage thresholds of the order of J/cm^2 but typically greater than 2 J/cm^2 for pulses that are hundreds of fs in duration [32]. For the lower fluence case, Fig. 7(b), the intensity-and-frequency-dependent PI rate is the strongest determinant of plasma generation at all wavelengths shown. These results support, for the continuum of pulse widths and wavelengths in the plotted range, the specific conclusions drawn from the propagation data shown in Figs. 2 and 3. For higher frequencies, photoionization will predominately determine the final ionization yield. For the NIR, the time and frequency dependence of ultrafast avalanching will predominate, but only at higher fluences.

4. TIME–FREQUENCY CONTROL OF PLASMA GENERATION

A. Modified MRE for Double-Pulses of Different Frequencies

Based on the time–frequency dependence of plasma generation observed in Fig. 7, this work proposes combining a low fluence, short pulse of high frequency followed by a higher fluence, longer pulse of low frequency into the material. The objective is to maximize plasma generation while minimizing the total fluence. This would be achieved by an initial high photoionization rate provided by a high-frequency "pre-pulse" followed by the efficient avalanching driven by the main lower frequency pulse. A variation of this method has been verified experimentally in several recent works [33–35]. However, the interpretation of such experiments depends on significant defect formation [34,35] to raise the photoionization rate, and this occurs largely on the time scale of picoseconds. What is investigated here is similar, but with ionization occurring strictly within the femtosecond time scale, thus avoiding significant defect formation during the field exposure.

The multi-rate equation is designed for a monochromatic laser field. If two laser fields of arbitrarily different frequencies (ω_1 and ω_2, orthogonally polarized) are present then a modification of the MRE is necessary. In this section a modified MRE is solved with an energy spacing of $\Delta\epsilon = \hbar\omega_1$, where $\omega_1 < \omega_2$. The modified MRE contributions resulting from the ω_1 field are thus the same as in Eq. (4). However, single-photon absorption events for the ω_2 field will not place electrons at proper intervals in the energy spacing based on ω_1. This treatment of the ω_2 single-photon absorption events is shown schematically in Fig. 8 and is described below.

The ratio of photon energies between the respective fields is given by $x = \hbar\omega_2/\hbar\omega_1$. Only an integer number of $\hbar\omega_2$ photons can be absorbed. Therefore, this model takes the integer $j = \langle x \rangle$, where $\langle\cdot\rangle$ denotes the integer part, and proportionally sends electrons promoted from the nth energy bin by ω_2 free-carrier absorption to the $n+j$ and the $n+j+1$ energy bins. The fraction of electrons promoted $j+1$ bins during one-photon absorption of $\hbar\omega_2$ is $f_u = x - j$. The fraction of electrons promoted j bins is then $f_d = 1 - f_u = 1 + j - x$. Note in Fig. 8 that $j = 2$ only as a hypothetical demonstration and corresponds to a combination of 1064 and 400 nm wavelength pulses.

The modeling of impact ionization must also be modified. Here again it is assumed that any single photon absorption event causing an electron to exceed the critical energy will immediately result in impact ionization. This modified MRE is represented mathematically for an electron population ρ_n as

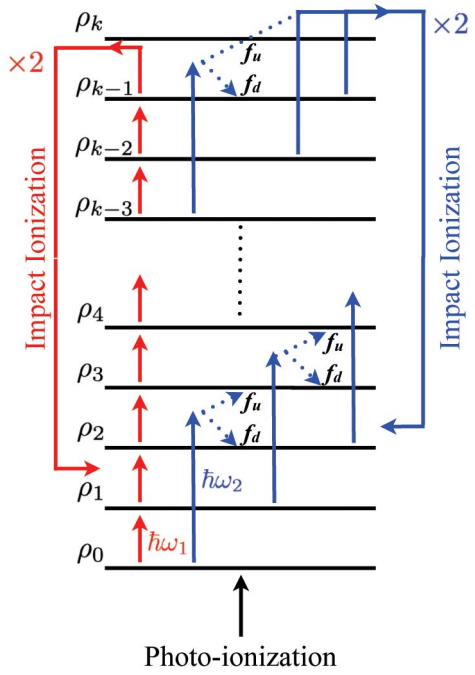

Fig. 8. Schematic of the multi-rate equation modified for two pulses of different frequencies.

$$\frac{d\rho_n}{dt} = [W_{\mathrm{PI}}(I_{\omega_1},\omega_1) + W_{\mathrm{PI}}(I_{\omega_2},\omega_2)]\delta_{n0} - \frac{\rho_n}{\tau_r} + W^{1\mathrm{pt}}_{\omega_1}[\rho_{n-1} - \rho_n + D_{nk}\rho_{k-1}] + W^{1\mathrm{pt}}_{\omega_2}[f_d\rho_{n-j} + f_u\rho_{n-j-1} - \rho_n] + W^{1\mathrm{pt}}_{\omega_2}\sum_{l=n+1}^{m} D_{nl}[f_d\rho_{l-j} + f_u\rho_{l-j-1}], \quad (6)$$

where the one-photon absorption rate is given by $W^{1\mathrm{pt}}_{\omega} = \sigma(\omega)I_{\omega}/\hbar\omega$. As before, ρ_n and its time rate of change are defined to be zero for all $n < 0$.

B. Multi-Frequency Seeded Ionization

Equation (6) is solved to simulate plasma generation by double-pulse fields. For this purpose, a low fluence, 50 fs (FWHM) pulse is combined with a high fluence 250 fs pulse. These two pulses are assumed to be Gaussian in time with respective peak intensities of 10^{12} W/cm^2 (50 fs pulse) and 4×10^{12} W/cm^2 (250 fs pulse). The delay separating these pulses is varied between 300 fs; thus, the field-material interactions remain on the ultrafast time scale. As an initial investigation, following the example of Refs. [34] and [35], an 800 nm field is combined with its third harmonic, 267 nm. Note that since ω_2 is a harmonic of ω_1, the fraction $f_u = 0$ and Eq. (6) reduces in this case to

$$\frac{d\rho_n}{dt} = [W_{\mathrm{PI}}(I_{\omega},\omega) + W_{\mathrm{PI}}(I_{3\omega},3\omega)]\delta_{n0} - \frac{\rho_n}{\tau_r} + W^{1\mathrm{pt}}_{\omega}[\rho_{n-1} - \rho_n + D_{nk}\rho_{k-1}] + W^{1\mathrm{pt}}_{3\omega}\left[\rho_{n-3} - \rho_n + \sum_{l=n+1}^{m} D_{nl}\rho_{l-3}\right]. \quad (7)$$

Plasma generation for the four possible combinations of these pulse widths and wavelengths was simulated. The results are shown in Fig. 9 as a function of time (the 250 fs pulse is centered at about time equal zero) and delay between the two pulses. Note that the plot for a pulse train of two 800 nm wavelength pulses is not shown because its peak ionization yield did not exceed 10^{18} cm^{-3}, the minimum scale of the other plots.

While high ionization yields are expected for the higher energy UV pulses, Fig. 9(a) indicates that one can also effectively generate a laser-induced plasma with a low-energy near-UV "pre-pulse" to seed photoionization before the main NIR pulse, as suggested in earlier works [11,34,35]. This seeding by the high-frequency pre-pulse causes the abrupt onset of ionization in Figs. 9(a) and 9(c) that occurs when the relative pulse delay approximately equals the time coordinate. Figures 9(b) and 9(c) show that the other possible combinations of pulse width and wavelength generate peak ionization yields that are about the same order of magnitude as the peak yield in Fig. 9(a). Note that in Figs. 9(b) and 9(c), the delay between the pulses has a comparatively smaller effect on the peak yield. In Fig. 9(a), the yields are more sensitive to the delay because avalanche ionization (driven by the high fluence, NIR pulses) is more sensitive to this delay. However, the highest yields in Fig. 9 occur for the pulse train consisting only of 267 nm pulses. Therefore, the combination of the 800 and 267 nm wavelengths is not the most effective ionization scheme investigated here.

The combination of an 800 nm field with one of its harmonics is convenient experimentally since both pulses can be derived from the same laser system. However, the advantages of multi-frequency control of plasma generation could be further increased by using a lower frequency for the high fluence pulse, since it will more effectively drive the avalanche process. For this reason, the simulations of Fig. 9 are performed again, but this time with wavelengths of 1064 and 267 nm, the results of which are shown in Fig. 10. Figures 9 and 10 are very similar in form. They differ primarily in that the plasma generated in the (a) and (b) subsets of Fig. 10 are increased compared to those of Fig. 9. In particular, the peak value of the plasma generated in Fig. 10(a) is over an order of magnitude

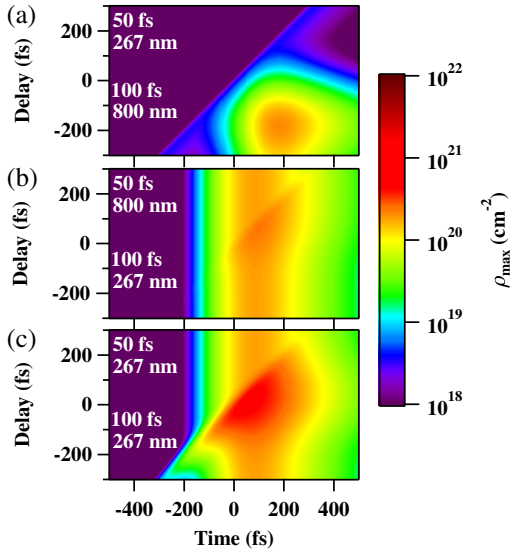

Fig. 9. Plasma generated in fused silica by 50–250 fs double-pulse trains as a function of time (given in the reference frame of the 250 fs pulse) and delay between the two pulses. The 50 and 250 fs pulses have wavelengths as labeled and respective peak intensities of 1×10^{12} W/cm^2 and 4×10^{12} W/cm^2.

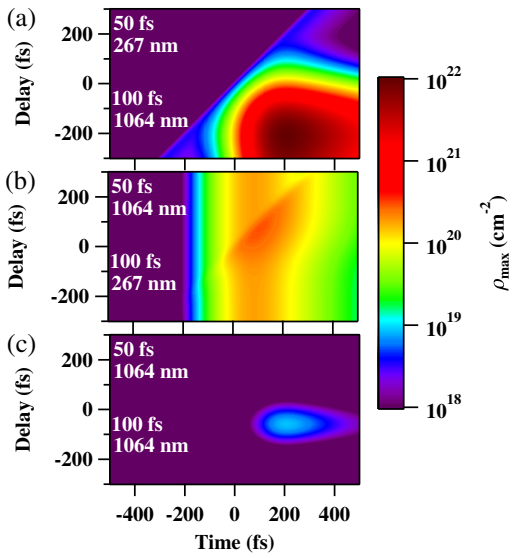

Fig. 10. Plasma generated in fused silica by 50–250 fs double-pulse trains as a function of time (given in the reference frame of the 250 fs pulse) and delay between the two pulses. The 50 and 250 fs pulses have wavelengths as labeled and respective peak intensities of 1×10^{12} W/cm^2 and 4×10^{12} W/cm^2.

larger than any of the other plots in Figs. 9 and 10. This pulse train scheme in Fig. 10(a) (although more difficult experimentally, requiring two different laser systems) would allow for much higher ionization yields, using much less fluence than corresponding single-pulse setups, and will continue to ensure that the ionization site is well-localized spatially.

5. CONCLUSION

The frequency dependence of plasma generation in dielectrics was examined for pulses of various intensities using a single rate equation coupled with pulse propagation simulations. These simulations reveal that pulses near the UV and in the NIR generate the largest ionization yields. In these simulations the plasma generated by 1064 and 800 nm wavelength pulses were the most effectively localized spatially along the propagation axis and beam dimensions, respectively.

Further simulations using a multi-rate equation model show that a delay in the avalanche effect for NIR pulses changes the resulting ionization yield by nearly an order of magnitude. Optimal frequency and pulse width conditions for single-pulse plasma generation are then determined for fields of high and low fluence using the multi-rate equation approach. Finally, a method for time–frequency control of plasma generation is tested by introducing a modified multi-rate equation to model ionization by double-pulses of different frequencies. This model shows how multi-chromatic double-pulse trains can control plasma generation with a minimal fluence using common laser frequencies. These simulations provide insight into more efficient and precise methods of modifying dielectric materials with ultrafast lasers.

ACKNOWLEDGMENTS

This work was supported by the Air Force Office of Scientific Research under grant FA9550-13-1-0069. The authors thank Thomas E. Lanier for useful discussions.

REFERENCES

1. L. Cerami, E. Mazur, S. Nolte, and C. B. Schaffer, "Femtosecond laser micromachining," in *Ultrafast Nonlinear Optics*, R. Thompson, C. Leburn, and D. Reid, eds. (Springer International Publishing, 2013), pp. 287–321.
2. C. B. Schaffer, A. Brodeur, and E. Mazur, "Laser-induced breakdown and damage in bulk transparent materials induced by tightly focused femtosecond laser pulses," Meas. Sci. Technol. **12**, 1784–1794 (2001).
3. R. R. Gattass and E. Mazur, "Femtosecond laser micromachining in transparent materials," Nat. Photonics **2**, 219–225 (2008).
4. D. von der Linde and H. Schuler, "Breakdown threshold and plasma formation in femtosecond laser-solid interaction," J. Opt. Soc. Am. B **13**, 216–222 (1996).
5. M. Kolesik, P. T. Whalen, and J. V. Moloney, "Theory and simulation of ultrafast intense pulse propagation in extended media," IEEE J. Sel. Top. Quantum Electron. **18**, 494–506 (2012).
6. P. Balling and J. Schou, "Femtosecond-laser ablation dynamics of dielectrics: basics and applications for thin films," Rep. Prog. Phys. **76**, 036502 (2013).
7. L. Englert, B. Rethfeld, L. Haag, M. Wollenhaupt, C. Sarpe-Tudoran, and T. Baumert, "Control of ionization processes in high band gap materials via tailored femtosecond pulses," Opt. Express **15**, 17855–17862 (2007).
8. E. Louzon, Z. Henis, S. Pecker, Y. Ehrlich, D. Fisher, M. Fraenkel, and A. Zigler, "Reduction of damage threshold in dielectric materials induced by negatively chirped laser pulses," Appl. Phys. Lett. **87**, 241903 (2005).
9. A. S. Arabanian and R. Massudi, "Study on effect of polarization and frequency chirp of incident pulse on femtosecond-laser-induced modification inside silica glass," J. Opt. Soc. Am. B **31**, 748–754 (2014).
10. L. Englert, M. Wollenhaupt, L. Haag, C. Sarpe-Tudoran, B. Rethfeld, and T. Baumert, "Material processing of dielectrics with temporally asymmetric shaped femtosecond laser pulses on the nanometer scale," Appl. Phys. A **92**, 749–753 (2008).
11. N. Bityurin and A. Kuznetsov, "Use of harmonics for femtosecond micromachining in pure dielectrics," J. Appl. Phys. **93**, 1567–1576 (2003).
12. R. R. Gattass, L. R. Cerami, and E. Mazur, "Micromachining of bulk glass with bursts of femtosecond laser pulses at variable repetition rates," Opt. Express **14**, 5279–5284 (2006).
13. J. Thomas, R. Bernard, K. Alti, A. Dharmadhikari, J. Dharmadhikari, A. Bhatnagar, C. Santhosh, and D. Mathur, "Pattern formation in transparent media using ultrashort laser pulses," Opt. Commun. **304**, 29–38 (2013).
14. D. Grojo, S. Leyder, P. Delaporte, W. Marine, M. Sentis, and O. Utéza, "Long-wavelength multiphoton ionization inside band-gap solids," Phys. Rev. B **88**, 195135 (2013).
15. A. Vogel, J. Noack, G. Huttman, and G. Paltauf, "Mechanisms of femtosecond laser nanosurgery of cells and tissues," Appl. Phys. B **81**, 1015–1047 (2005).
16. J. Dai, B. Clough, I.-C. Ho, X. Lu, J. Liu, and X.-C. Zhang, "Recent progresses in terahertz wave air photonics," IEEE Trans. Terahertz Sci. Technol. **1**, 274–281 (2011).
17. B. C. Stuart, M. D. Feit, S. Herman, A. M. Rubenchik, B. W. Shore, and M. D. Perry, "Nanosecond-to-femtosecond laser-induced breakdown in dielectrics," Phys. Rev. B **53**, 1749–1761 (1996).
18. L. V. Keldysh, "Ionization in the field of a strong electromagnetic wave," Sov. Phys. JETP **20**, 1307–1314 (1965).
19. A. Q. Wu, I. H. Chowdhury, and X. Xu, "Femtosecond laser absorption in fused silica: numerical and experimental investigation," Phys. Rev. B **72**, 085128 (2005).
20. J. R. Gulley and W. M. Dennis, "Ultrashort-pulse propagation through free-carrier plasmas," Phys. Rev. A **81**, 033818 (2010).
21. A. Kaiser, B. Rethfeld, M. Vicanek, and G. Simon, "Microscopic processes in dielectrics under irradiation by subpicosecond laser pulses," Phys. Rev. B **61**, 11437–11450 (2000).
22. S. W. Winkler, I. M. Burakov, R. Stoian, N. M. Bulgakova, A. Husakou, A. Mermillod-Blondin, A. Rosenfeld, D. Ashkenasi, and I. V. Hertel, "Transient response of dielectric materials exposed to ultrafast laser radiation," Appl. Phys. A **84**, 413–422 (2006).

23. E. S. Efimenko, Y. A. Malkov, A. A. Murzanev, and A. N. Stepanov, "Femtosecond laser pulse-induced breakdown of a single water microdroplet," J. Opt. Soc. Am. B **31**, 534–541 (2014).
24. K. Waedegaard, D. Sandkamm, L. Haahr-Lillevang, K. Bay, and P. Balling, "Modeling short-pulse laser excitation of dielectric materials," Appl. Phys. A **117**, 7–12 (2014).
25. V. Kudriagov, E. Gaizauskas, and V. Sirutkaitis, "Beam transformation and permanent modification in fused silica induced by femtosecond filaments," J. Opt. Soc. Am. B **22**, 2619–2627 (2005).
26. L. Bergé, S. Skupin, R. Nuter, J. Kasparian, and J.-P. Wolf, "Ultrashort filaments of light in weakly ionized, optically transparent media," Rep. Prog. Phys. **70**, 1633–1713 (2007).
27. B. Rethfeld, "Free-electron generation in laser-irradiated dielectrics," Phys. Rev. B **73**, 035101 (2006).
28. B. Rethfeld, "Unified model for the free-electron avalanche in laser-irradiated dielectrics," Phys. Rev. Lett. **92**, 187401 (2004).
29. B. C. Stuart, M. D. Feit, A. M. Rubenchik, B. W. Shore, and M. D. Perry, "Laser-induced damage in dielectrics with nanosecond to subpicosecond pulses," Phys. Rev. Lett. **74**, 2248–2251 (1995).
30. B. H. Christensen and P. Balling, "Modeling ultrashort-pulse laser ablation of dielectric materials," Phys. Rev. B **79**, 155424 (2009).
31. D. Giguère, G. Olivié, F. Vidal, S. Toetsch, G. Girard, T. Ozaki, J.-C. Kieffer, O. Nada, and I. Brunette, "Laser ablation threshold dependence on pulse duration for fused silica and corneal tissues: experiments and modeling," J. Opt. Soc. Am. A **24**, 1562–1568 (2007).
32. J. R. Gulley, S. W. Winkler, W. M. Dennis, C. M. Liebig, and R. Stoian, "Interaction of ultrashort-laser pulses with induced undercritical plasmas in fused silica," Phys. Rev. A **85**, 013808 (2012).
33. A. Mouskeftaras, S. Guizard, N. Fedorov, and S. Klimentov, "Mechanisms of femtosecond laser ablation of dielectrics revealed by double pump-probe experiment," Appl. Phys. A **110**, 709–715 (2013).
34. X. Yu, Q. Bian, B. Zhao, Z. Chang, P. B. Corkum, and S. Lei, "Near-infrared femtosecond laser machining initiated by ultraviolet multiphoton ionization," Appl. Phys. Lett. **102**, 101111 (2013).
35. X. Yu, Q. Bian, Z. Chang, P. B. Corkum, and S. Lei, "Femtosecond laser nanomachining initiated by ultraviolet multiphoton ionization," Opt. Express **21**, 24185–24190 (2013).